Empirical modeling of plasma sheet pressure and three-dimensional force-balanced magnetospheric magnetic field structure: 1. Observation

Chih-Ping Wang,[1] Chao Yue,[1] Sorin Zaharia,[2] Xiaoyan Xing,[1] Larry Lyons,[1] Vassilis Angelopoulos,[3] Tsugunobu Nagai,[4] and Tony Lui[5]

Received 12 April 2013; revised 16 September 2013; accepted 20 September 2013.

[1] A three-dimensional (3-D) magnetic field configuration in force balance with a realistic plasma pressure distribution can provide more accurate evaluation of the role of magnetic field on plasma sheet dynamics and M-I coupling. We used Geotail and Time History of Events and Macroscale Interactions During Substorms (THEMIS) data to establish an empirical model for nightside equatorial isotropic plasma pressure to $r = 30\ R_E$ for $Kp = 0$–5 and for solar wind dynamic pressure (P_{SW}) = 1.5 and 3 nPa. The model pressure is used in the companion paper for modeling a 3-D force-balanced pressure and magnetic field equilibrium. Larger convection during higher *Kp* drives the plasma sheet further earthward, resulting in larger increase of pressure and pressure gradient at smaller radial distance. On the other hand, magnetosphere compression by increasing P_{SW} enhances pressure and pressure gradient mainly in the tail plasma sheet. While both pressure and radial gradients are enhanced with increasing *Kp* or P_{SW}, there is no significant azimuthal pressure variation statistically under all *Kp* and P_{SW} conditions. The empirical pressures well reproduce these statistical profiles with very high correlation coefficients. Additionally, comparisons with pressure gradients computed using two simultaneous measurements from two THEMIS spacecraft show reasonable agreement. Furthermore, our model provides more accurate pressure gradients than previous empirical models. The model magnetic field distributions obtained in the companion paper from requiring force balance with these empirical pressure profiles are also found to be consistent with the magnetic field observations, indicating that our equilibria well represent realistic 3-D pressure and magnetic field configurations.

Citation: Wang, C.-P., C. Yue, S. Zaharia, X. Xing, L. Lyons, V. Angelopoulos, T. Nagai, and T. Lui (2013), Empirical modeling of plasma sheet pressure and three-dimensional force-balanced magnetospheric magnetic field structure: 1. Observation, *J. Geophys. Res. Space Physics*, *118*, doi:10.1002/jgra.50585.

1. Introduction

[2] Ions and electrons in the nightside magnetosphere, driven by the dawn-to-dusk convection electric field, flow earthward and are energized, resulting in an increase in plasma pressure. Compression of the magnetosphere by larger solar wind dynamic pressure can also enhance magnetosphere plasma pressure. Most of the time, the flow is slow [e.g., *Angelopoulos et al*., 1994; *Wang et al*., 2009] so that magnetic field configuration changes to maintain force balance with the increased pressure. Increasing plasma pressure gradient in the radial direction causes stretching of magnetic field and enhanced perpendicular currents flowing azimuthally. On the other hand, field-aligned currents (FACs) associated with the azimuthal pressure gradient flow into or out of the ionosphere, resulting in bending of magnetic field lines. Thus, the pressure spatial distribution plays an essential role in determining the magnetic configuration in the near-Earth magnetosphere and this coupling is crucial to geomagnetic disturbances. However, current empirical plasma pressure and magnetic field models do not provide force-balanced configurations. As described in the companion paper (C. Yue *et al*., Empirical modeling of three-dimensional force-balanced pressure and magnetic field equilibrium in the near-Earth magnetosphere: 2. Modeling, submitted to *Journal of Geophysical Research*, 2013, hereinafter Paper 2), the goal of this study is to establish realistic 3-D pressure and magnetic field configurations that satisfy the physical principle of force balance. In this paper, we analyzed the pressure and magnetic field observations from Geotail and Time History of Events and Macroscale

[1]Department of Atmospheric and Oceanic Sciences, UCLA, Los Angeles, California, USA.
[2]Space Science and Applications, Los Alamos National Laboratory, Los Alamos, New Mexico, USA.
[3]Department of Earth and Space Science, UCLA, Los Angeles, California, USA.
[4]Earth and Planetary Sciences I2-5, Tokyo Institute of Technology, Tokyo, Japan.
[5]Applied Physics Laboratory, Johns Hopkins University, Laurel, Maryland, USA.

Corresponding author: C.-P. Wang, Department of Atmospheric and Oceanic Sciences, UCLA, Los Angeles, CA, USA. (cat@atmos.ucla.edu)

2169-9380/13/10.1002/jgra.50585

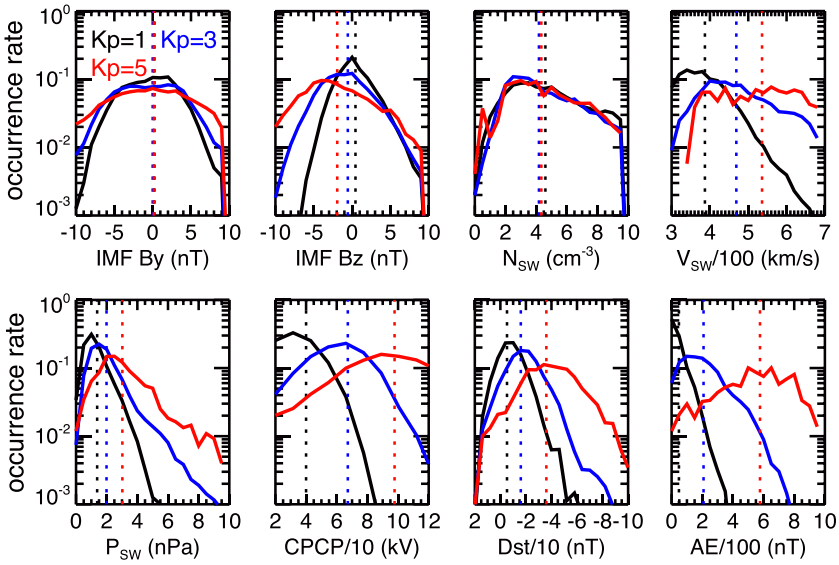

Figure 1. Occurrence rate for the IMF B_y, IMF B_z, solar wind density (N_{sw}), solar wind speed (V_{sw}), solar wind dynamic pressure (P_{sw}), the cross polar cap potential (CPCP), Dst, and AE for $Kp = 1$ (the black curves), 3 (the blue curves), and 5 (the red curves). The cross polar cap potential drop is estimated using the Weimer empirical model [*Weimer*, 1995]. The vertical dotted lines indicate median values.

Interactions During Substorms (THEMIS) and established an empirical pressure model that provides the realistic pressure inputs needed for the magnetic field modeling presented in Paper 2. In addition, we evaluated the model magnetic field by comparing with the observations.

[3] Plasma pressure in the plasma sheet is several tenths of nPa [e.g., *Huang and Frank*, 1986] and increases to several nPa in the inner magnetosphere [e.g., *Lui and Hamilton*, 1992; *De Michelis et al*., 1999; *Kirpichev and Antonova*, 2011]. The pressure depends on the conditions of the solar wind and interplanetary magnetic field (IMF) [e.g., *Wang et al*., 2007]. Among all solar wind parameters, the solar wind dynamic pressure (P_{SW}) is found to strongly regulate the plasma sheet pressure [*Borovsky et al*., 1998]. The pressure also varies significantly during geomagnetic disturbances [e.g., *Baumjohann et al*., 1991; *Kistler et al*., 1992]. Highly isotropic pressure is commonly observed in the tail plasma sheet [e.g., *Kaufmann et al*., 2002; *Wang et al*., 2011], but pressure becomes anisotropic in the inner magnetosphere with larger pressure in the perpendicular direction [e.g., *De Michelis et al*., 1999]. Electron pressure is generally small compared with ion pressure in the tail plasma sheet ($< \sim 1/6$) [e.g., *Wang et al*., 2009] but becomes much larger toward smaller radial distance. The pressure spatial distribution has been investigated observationally using either in situ measurements [e.g., *Spence et al*., 1989; *Guild et al*., 2004; *Kaufmann et al*., 2004; *Wang et al*., 2007] or ionosphere observations [*Wing and Newell*, 1998], and many simulations have been conducted to understand the underlying plasma dynamics responsible for the distribution.

[4] To construct a realistic force-balanced magnetic field configuration requires knowing the pressure spatial distribution. A few empirical pressure models have been developed to describe the spatial distribution. *Spence and Kivelson* [1993] developed an analytical form for the midnight pressure profile from the tail to the inner magnetosphere during quiet times. Using Geotail data, *Tsyganenko and Mukai* [2003] established a 2-D model for plasma pressure with dependence on the IMF and P_{SW} for the region of $r = 10$ to 30 R_E. Since 2007, five spacecraft from THEMIS mission have extensively surveyed plasma pressure near the equator in the region of $r \sim 2$ to 12 R_E. This, together with more than 10 years of Geotail observations from r ~8 to 30 R_E, provides us an excellent data set to establish a 2-D empirical pressure profile from the plasma sheet to the inner magnetosphere.

[5] In this paper we develop analytic descriptions of the plasma pressure at the equator for different levels of *Kp* and *P*sw. In section 2, we described our methods to obtain the best estimate of plasma pressure at the center of the current sheet. This allows us to specify more accurate pressure gradients for our magnetic field modeling than can be given by the previous empirical pressure models. We present in section 3 our empirical pressure profiles and evaluate them against statistical pressure distributions as well as the pressure gradients obtained by using simultaneous measurements from two of the THEMIS spacecraft. We also compare our model profiles with those of the previous models and discuss the factors contributing to the differences. Finally, we evaluate the 3-D plasma and magnetic field equilibrium obtained in Paper 2 against statistical profiles.

2. Empirical Pressure Model

[6] The objective of this paper is to establish an empirical model for 2-D distributions of plasma pressure at the equator as a function of *Kp* and the solar wind dynamic pressure (P_{SW}). We chose *Kp* over other indices because it indicates global magnetosphere activity, which corresponds to global changes in the plasma and magnetic field configurations. As shown in Figure 1, higher *Kp* well indicates larger solar wind driving (as shown by higher cross polar cap potential)

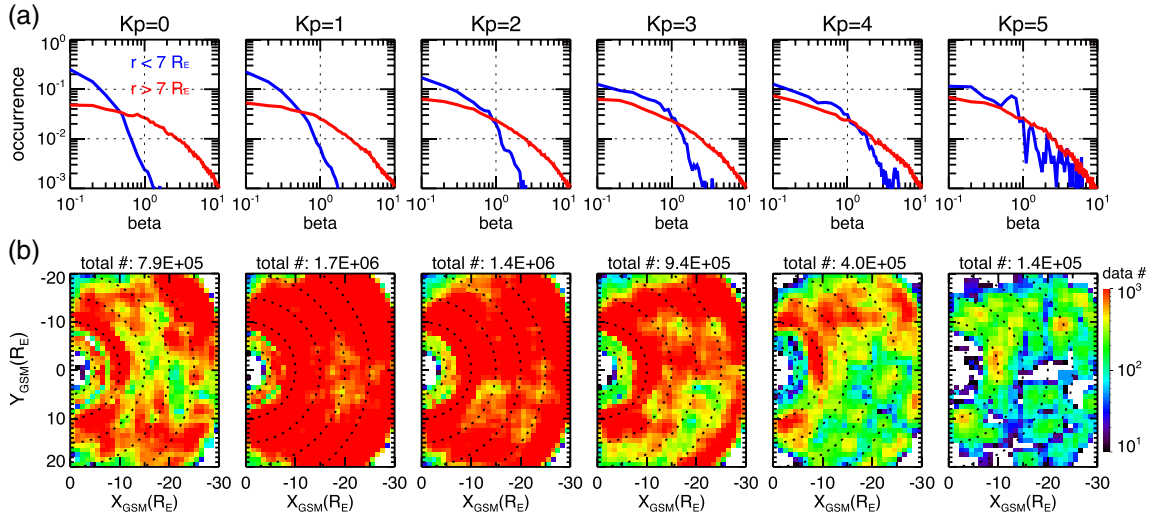

Figure 2. (a) Occurrence rates of the plasma beta for the Geotail and THEMIS measurements on the nightside for different *Kp* levels. (b) The equatorial distributions of the number of measurements satisfying the selection criteria for different *Kp* levels. The number above each plot is the total number of measurements for each *Kp* level.

as well as more active magnetosphere responses in the inner magnetosphere (more negative *Dst*) and in the plasma sheet (higher *AE*). The lower *Dst* is caused by stronger ring current, and thus more substantial magnetic field changes, in the inner magnetosphere. Higher *AE* indicates stronger ground disturbance around the auroral zone connecting to the plasma sheet, which is mainly attributed to the enhanced ionospheric and field-aligned currents. *Kp* is also found to be well correlated with the ionosphere isotropic precipitation boundary [*Newell et al.*, 1998], which has been shown to give good indication of magnetic field line stretching [*Sergeev and Gvozdevsky*, 1995].

2.1. Observational Data

[7] In this study we use Geotail data from 1 January 1995 to 31 December 2005 (data after 2006 are not used since Geotail stayed mostly at high latitudes in the magnetotail after 2006) and THEMIS data from 23 March 2007 to 30 April 2010. Aberrated geocentric solar magnetospheric coordinates (with the aberration angle determined by 1 h averaged solar wind velocity) are used. Geotail covers regions from r ~8 to 30 R_E. In our selected THEMIS periods, three of the five THEMIS spacecraft cover regions inside r ~12 R_E, while the other two cover regions inside r ~30 R_E. Therefore, by combining these two data sets, we obtain observations of the magnetosphere from r ~30 R_E on the nightside to the dayside magnetopause. Plasma data from two instruments aboard Geotail are used: The ion and electron data from the low energy particle (LEP) instrument [*Mukai et al.*, 1994] that covers the ion energy range from 21 eV/q to 44 keV/q and the electron energy range from 43 eV to 41 keV, and the proton data from the energetic particles and ion composition (EPIC) instrument [*Williams et al.*, 1994] that covers the ion energy range from 46 to 3005 keV (EPIC only measures 32 and > 110 keV integral electrons so electron moments are not available). Magnetic field data are from the magnetic field experiment [*Kokubun et al.*, 1994]. The ion moments are from a summation of the LEP and EPIC data, and the electron moments are from the LEP data. One minute averages of the Geotail plasma and magnetic field data are used.

[8] For THEMIS, the ions and electrons are measured by an electrostatic analyzer (ESA, 0.006–20 keV/q for ions and 0.007–26 keV for electrons) [*McFadden et al.*, 2008] and a solid state telescope (SST, 35 keV–6 MeV for ions and 30 keV–6 MeV for electrons). Full distributions are used with time resolution of a few minutes. The total plasma moments are a summation of the ESA and SST moments. The magnetic field is measured by the Flux Gate Magnetometer (FGM) instrument [*Auster et al.*, 2008]. Sunlight contamination to the SST is removed. The penetrating radiation contamination is removed from the ESA data by subtracting the minimum count value within the ESA energy ranges (see *Wang et al.* [2011] for more details). However, there is no reliable method to remove the penetrating radiation contamination to the SST. Since SST pressure becomes dominant with decreasing radial distance, pressure becomes less reliable inside r ~7 R_E where radiation contamination may be stronger. For ions, there is energy gap (from ~20 to 28 keV) between the highest ESA channel and the lowest SST channel. We interpolate the fluxes for this energy gap using the fluxes from the two nearby energy channels. For both Geotail and THEMIS, plasma pressure is a summation of ion and electron plasma pressure (note that Geotail only provides electron pressure from electrons below 40 keV, but pressure contribution from > 40 keV electrons is negligible even in the inner magnetosphere). The plasma pressure is assumed isotropic.

[9] Note that there is no time overlap for the selected Geotail and THEMIS data. The overall THEMIS fluxes in the spatial overlap region are found to be smaller than the Geotail fluxes (up to a factor of 2), likely due to the solar wind density during the selected THEMIS period (average ~4 cm^{-3}) being lower than that during the selected Geotail period (average ~6.5 cm^{-3}). Nevertheless, the effect of P_{SW} on the plasma pressure is corrected when normalizing the pressure to a fixed P_{SW}. The solar wind parameters used in this study are from OMNI data, which have been propagated to the nose of the Earth's bow shock.

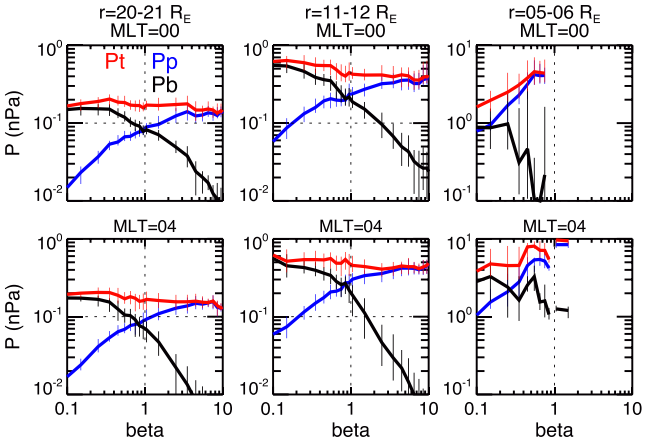

Figure 3. Total pressure (the red curves), plasma pressure (the blue curves), and magnetic pressure (the black curves) as a function of plasma beta at different radial distances and MLTs.

2.2. Selection Criteria

[10] The equatorial plane is the center of current sheet where the radial component of magnetic field reverses its direction. At a fixed (X, Y) location, plasma pressure (P_p) is normally the largest while total magnetic pressure ($P_{b,t}=\sqrt{(B_x^2+B_y^2+B_z^2)}/2\mu_0$) is the smallest at the equatorial plane. With increasing Z distance from the current sheet, the plasma pressure decreases while total magnetic pressure increases, resulting in a decrease in the plasma beta ($P_p/P_{b,t}$). Since it is not possible to determine the actual Z distance to the current sheet from a single point observation, the plasma beta is often used to indicate how far a satellite is away from the current sheet. Considering the force balance in the Z direction discussed in the next paragraph, in the plasma sheet where magnetic field lines are generally stretched, the plasma pressure measured by a satellite in a region of smaller plasma beta should be smaller than the plasma pressure right at the center of current sheet (equatorial plasma pressure, $P_{p,eq}$) where the plasma beta is the largest at the same (X, Y) location. Figure 2a shows the occurrence rates of plasma beta measured by THEMIS and Geotail. The much lower occurrence rates of high plasma beta (= 10) indicate that it is rare for THEMIS and Geotail to be exactly on the equatorial plane despite both satellite orbits being near the equatorial plane. Therefore, it is difficult to obtain sufficient measurements of $P_{p,eq}$ for statistical analysis. Nevertheless, based on the following argument, we can use the measurement away from the current sheet to estimate $P_{p,eq}$.

[11] From the force balance equation, $\nabla P_p = 1/\mu_0\,(\nabla\times\mathbf{B})\times\mathbf{B}$, in the Z direction, one can obtain $P_p + P_b - 1/\mu_0 \int_0^z (\partial B_z/\partial x \cdot B_x + \partial B_z/\partial y \cdot B_y)dz = P_{p,eq}$, where $P_b=\sqrt{(B_x^2+B_y^2)}/2\mu_0$ is the radial magnetic pressure (note that P_b has no B_z component so that it is different from $P_{b,t}$), and $(1/\mu_0 \int_0^z (\partial B_z/\partial x \cdot B_x + \partial B_z/\partial y \cdot B_y)dz)$ is the magnetic curvature term. If the magnetic curvature term is zero, then total pressure $P_t = P_p + P_b$ at a fixed (X, Y) location should be a constant in the Z direction, thus is independent of the plasma beta. The magnetic curvature term is in general very small in the vicinity of the current sheet but becomes larger with increasing Z distance (decreasing plasma beta) and is larger in a more dipolar field.

[12] Figure 3 shows how P_p, P_b, and P_t change with the plasma beta at different radial distances and MLTs. In general, in the region outside $r\sim 7\ R_E$ and when the plasma beta is larger 1, P_t is almost independent of the plasma beta and is quite close to $P_{p,eq}$, while P_p decreases substantially with decreasing plasma beta. Therefore, in this study, in the region outside of $r = 7\ R_E$, we selected data only when the plasma beta ≥ 1 and assumed that the observed P_t is equal to $P_{p,eq}$. As shown in Figure 2a, inside $r\sim 7\ R_E$, with decreasing r, the plasma beta decreases quickly to below 1 because of sharply increasing magnetic field strength. Figure 3 shows that inside $r\sim 7\ R_E$, both P_t and P_p decrease with decreasing plasma beta because of increasing curvature term, but the decrease of P_t is much less significant than that of P_p. Thus, for $r < 7\ R_E$, we only selected P_t with the plasma beta ≥ 0.1 and used it to represent $P_{p,eq}$, with the caution that this leads to underestimates of the actual $P_{p,eq}$. These plasma beta lower limits were so chosen in order to obtain as best estimate of $P_{p,eq}$ as possible and to collect sufficient data points for establishing a spatial distribution of $P_{p,eq}$ with statistical significance. Additionally, to avoid periods of fast flows when the above force balance assumption is less valid, we included only data with perpendicular and parallel plasma bulk flow smaller than 100 km/s. The equatorial distributions of the number of data selected with these criteria for different Kp levels are shown in Figure 2b. Since occurrence of higher Kp is less frequent, the data number for $Kp = 5$ is significantly smaller than those of lower Kp levels.

[13] As shown by *Borovsky et al.* [1998], the plasma sheet P_p is highly correlated with P_{SW}. We found that the correlation between P_t and P_{SW} is even higher than that between P_p and P_{SW}. However, the P_{SW} correlation for P_p or P_t is not the same throughout the plasma sheet. Figure 4 shows that a better correlation is found at larger $|Y|$ and at larger radial distance. The correlation weakens with decreasing r, and generally, no clear correlation is found inside $r\sim 7\ R_E$. To approximately correct the effect of P_{SW} in order to obtain a spatial P_t distribution corresponding to the same P_{SW}, we first did a linear power law fit to the correlation between P_t and P_{SW} within each 1 $R_E \times 1\ R_E$ X-Y area. Using the fit, we then obtained normalized P_t ($P_{t,n}$) corresponding to two P_{SW} levels: $P_{SW} = 1.5$ and $P_{SW} = 3$ nPa. This normalization was done for all areas outside $r = 7\ R_E$ (so inside $r = 7\ R_E$, $P_{t,n}$ is the same as the observed P_t). Finally, we sorted $P_{t,n}$ to six Kp levels from $Kp = 0$ to 5 (there were not enough data for $Kp > 6$).

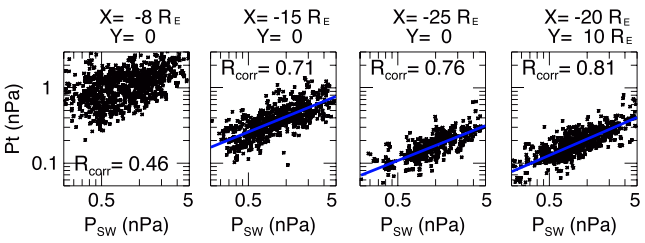

Figure 4. Total pressure as a function of the solar wind dynamic pressure at different X-Y locations. R_{corr} indicates the linear correlation coefficients.

Table 1. Values of Fitting Parameters b1 to b9 for P_m in Equation (1) for Different Kp and $P_{SW} = 1.5$ nPa[a]

	$Kp = 0$	$Kp = 1$	$Kp = 2$	$Kp = 3$	$Kp = 4$	$Kp = 5$
	$P_{SW} = 1.5$	$P_{SW} = 1.5$	$P_{SW} = 1.5$	$P_{SW} = 1.5$	$P_{SW} = 1.5$	$P_{SW} = 1.5$
b1	−0.8700	−0.7890	−0.7888	−0.6887	−0.6590	−0.7311
	±0.0484	±0.0565	±0.0639	±0.0657	±0.1408	±0.1161
b2	213.5363	123.7894	73.3651	99.6864	60.2186	137.1203
	±36.7470	±26.1173	±30.6172	±23.4886	±35.6205	±511.8743
b3	0.0322	−0.1999	38.6285	−5.7370	−27.2739	166.9548
	±8.4077	±1.5009	±1.8424	±1.3305	±1.4691	±9.4334
b4	99.2106	73.8102	99.9520	15.4089	29.3575	231.5938
	±26.9372	±24.8810	±38.5686	±12.4035	±27.6130	±441.4238
b5	−1.2410	−1.2334	−2.0651	−1.2622	−1.5970	−1.7076
	±0.6442	±0.8023	±0.3870	±0.8439	±0.1755	±0.8687
b6	7.3564	11.2507	69.7594	15.3724	39.4608	53.7482
	±1.5667	±3.0741	±4.7404	±2.8034	±18.0344	±132.4751
b7	−0.5093	0.0502	0.2883	0.0242	1.3241	−3.5660
	±0.0855	±0.1339	±0.1741	±0.1715	±0.3648	±1.2279
b8	2.0266	−0.0773	9.8675	0.2230	−4.0530	−12.5359
	±0.2359	±0.3020	±0.3484	±0.3125	±1.5940	±8.138
b9	0.0056	−0.0611	0.0787	−0.0864	−0.0393	0.0104
	±0.8397	±0.9703	±0.3038	±0.4947	±0.1880	±0.2769
R_{corr}	0.94402	0.93681	0.9255	0.93407	0.87015	0.85403
Err_{RMS}	0.028	0.033	0.032	0.036	0.034	0.034
Err_{Mean}	0.102	0.093	0.112	0.131	0.124	0.236

[a] R_{corr} is the linear correlation coefficient between P_m and $P_{t,n}$. Err_{RMS} is the normalized RMS error. Err_{Mean} is the normalized mean error.

2.3. Pressure Model

[14] To obtain an analytical spatial distribution for the equatorial plasma pressure, we fitted $P_{t,n}$ to a model pressure (P_m) with nine fitting parameters (b1 to b9),

$$Pm(r,\varphi)(\text{nPa}) = e^{b1\,r}\left[b2 + b3\sin(\varphi) + b4\sin^2(\varphi)\right] + r^{b5}\left[b6 + b7\sin(\varphi) + b8\sin^2(\varphi)\right] + b9, \quad (1)$$

where r is the radial distance in R_E and φ is the azimuthal angle (0° at noon, 90° at dusk, 180° at midnight, and 270° at dawn). b1 to b4 mainly control the pressure in the inner magnetosphere while b5 to b9 determine the plasma sheet pressure.

[15] The parameters for the best fit were obtained by minimizing the difference between $P_{t,n}$ and P_m using the Matlab fminsearch function, which uses the Nelder-Mead simplex algorithm as described in *Lagarias et al*. [1998] to find the minimum of a scalar function of several variables starting with an initial estimate. The scalar function in our case is defined as $\Sigma[\text{weight}\cdot(P_m - P_{t,n})^2]$, where weight is the number of measurements within each (X, Y) bin/total number of the measurements. Different initial estimates can give different fitting profiles but with quite similar correlation coefficients and fitting errors between $P_{t,n}$ and P_m. A profile

Table 2. Values of Fitting Parameters b1 to b9 for P_m in Equation (1) for Different Kp and $P_{SW} = 3$ nPa[a]

	$Kp = 0$	$Kp = 1$	$Kp = 2$	$Kp = 3$	$Kp = 4$	$Kp = 5$
	$P_{SW} = 3$	$P_{SW} = 3$	$P_{SW} = 3$	$P_{SW} = 3$	$P_{SW} = 3$	$P_{SW} = 3$
b1	−0.9072	−0.9024	−0.8432	−0.8264	−0.6909	−0.7906
	±0.0518	±0.0602	±0.0669	±0.0811	±0.3460	±0.1316
b2	240.0024	152.1005	65.3578	109.6771	8.1615	188.7615
	±47.0330	±31.7535	±34.2491	±31.4862	±82.7838	±84.8879
b3	−2.8333	2.6496	−63.4070	−6.4229	−31.6261	209.6659
	±4.6522	±2.4269	±1.1343	±0.2219	±0.3266	±3.6729
b4	135.1886	126.1990	172.1954	25.9049	43.7472	218.4614
	±39.0879	±37.2681	±52.6818	±15.8282	±74.4886	±167.0783
b5	−0.4292	−1.2436	−1.5136	−1.5213	−1.7950	−1.7408
	±0.1658	±0.5513	±0.2516	±0.5247	±0.2437	±0.3538
b6	3.7857	16.7792	34.4588	39.0839	88.8841	76.1308
	±1.2484	±7.8300	±2.0089	±21.9181	±33.9701	±24.6083
b7	−0.0752	−0.0745	0.6017	−0.5118	1.3109	−2.8949
	±0.0976	±0.2987	±0.2004	±0.4317	±1.7290	±1.5301
b8	0.2609	−0.1996	−2.5027	0.0237	−11.9868	−15.0630
	±0.5078	±0.5059	±0.4430	±0.7579	±0.8781	±3.8129
b9	−0.7513	−0.0718	0.0093	−0.0090	0.0306	0.1342
	±0.7740	±0.7139	±0.5570	±0.0205	±0.0818	±0.1815
R_{corr}	0.93959	0.93112	0.92439	0.932	0.86305	0.83832
Err_{RMS}	0.029	0.034	0.033	0.037	0.035	0.033
Err_{Mean}	0.096	0.088	0.129	0.136	0.132	0.375

[a] R_{corr} is the linear correlation coefficient between P_m and $P_{t,n}$. Err_{RMS} is the normalized RMS error. Err_{Mean} is the normalized mean error.

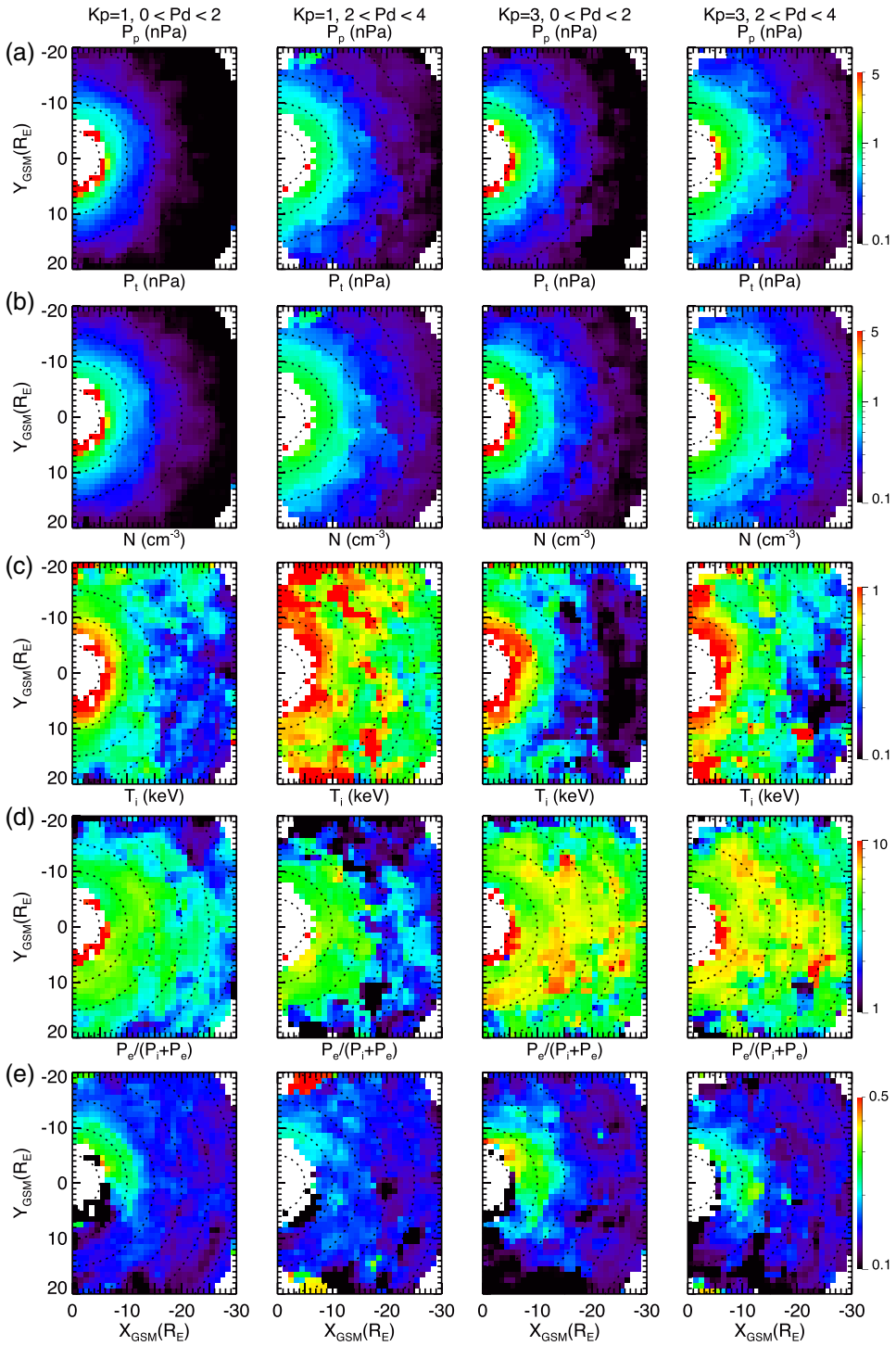

Figure 5. Equatorial distributions of (a) plasma pressure, (b) total pressure, (c) number density, (d) ion temperature, and (e) electron to total plasma pressure ratio for four different Kp and P_{SW} ranges.

with lower fitting error may not necessarily give better overall representation of the observed profile because the lower error may simply be a result of better fitting in more localized region. Thus, for each $Kp-P_{SW}$ pressure distributions, we first conducted the fitting with many initial estimates. We then visually compared the fitted profiles with the observations and selected the one that gives the best large-scale representation. The values of the fitting parameters and the errors (90% confidence intervals) for each parameter estimated using the bootstrap method for different Kp are listed in Tables 1 and 2 for $P_{SW} = 1.5$ and 3 nPa, respectively, together with the linear correlation coefficients and the root-mean-square (RMS) and mean fitting errors. The correlation coefficients for the $Kp = 5$ pressure are lower, and errors are substantially larger because of relatively fewer available data than for the lower Kp cases.

[16] Note that our goal is to use one analytical function to give model representatives of observed large-scale pressure

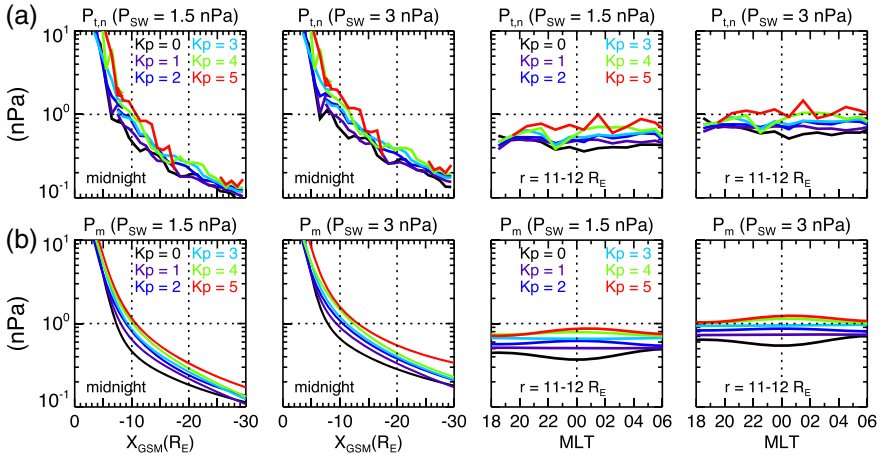

Figure 6. The radial profiles at midnight (the left two columns) and azimuthal profiles at $r = 11$–$12\ R_E$ (the right two columns) of (a) the observed pressure, $P_{t,n}$, and (b) the model pressure, P_m, for $P_{SW} = 1.5$ and 3 nPa and $Kp = 0$ to 5.

distribution for different Kp and P_{SW} levels and use these model pressures for constructing force-balanced magnetic field configuration presented in Paper 2. The function is certainly not unique, and the function terms do not have to be orthogonal to each other. We have tested many function forms, including those having only orthogonal terms, such as $\sin(\varphi)$ and $\cos(\varphi)$, or terms of higher order, such as $\sin^3(\varphi)$. Among the tests, the function (1) is the one that has smallest overall fitting errors for all the Kp and P_{SW} levels. The values of each fitting parameters do not present actual physical meaning of pressure and are not found to change regularly with increasing Kp or P_{SW}. It is the summation of all parameters that gives the meaningful model pressure profiles. Therefore, despite that some of the fitting parameters may have large jumps in their values between neighboring Kp or P_{SW} cases, P_m does not have such jumps and it changes systematically with increasing Kp and P_{SW} as shown in section 3.

3. Results and Discussion

[17] In this section, we focus our investigation on four different cases: $Kp = 1$ and 3 together with $P_{SW} = 1.5$ and 3 nPa.

3.1. Equatorial Pressure Distributions

[18] Figure 5 shows the unnormalized total pressure (P_t), plasma density (N), and ion temperature (T_i) for $Kp = 1$ and 3 within two P_{SW} ranges ($0 < P_{SW} \le 2$ nPa and $2 < P_{SW} \le 4$ nPa). As Kp increases from 1 to 3, the overall T_i increases (in the region $-10 < X < -30\ R_E$ and $|Y| < 15\ R_E$) by a factor of ~1.7 to 2.4 while N decreases by a factor of ~0.66 to 0.78. As a result of the opposite N and T_i changes, P_t only becomes slightly higher (a factor of < 1.2). The higher T_i during higher Kp is likely due to larger particle energization by stronger solar wind driving and convection electric field, as indicated by the higher cross polar cap potential drop at higher Kp shown in Figure 1. The decrease in N, on the other hand, is possibly due to stronger convection pushing the colder plasma sheet population toward the two flanks [*Wang et al.*, 2010]. The changes due to P_{SW} are quite different from the Kp effect. As P_{SW} increases by a factor of 2, the overall N increases by a factor of 2 to 2.5 while T_i changes only slightly by a factor of 0.8 to 1, resulting in an increase of P_t by a factor of ~1.6. The higher plasma sheet density and pressure is mainly a result of magnetosphere compression by the higher P_{SW}.

[19] Figure 5d shows that electron contribution to the total plasma pressure increases with decreasing r. The electron pressure becomes important (> 0.2 of the total plasma pressure) inside $r \sim 15\ R_E$ and is more significant in the post midnight than premidnight sector due to dawnward magnetic drift of higher energy electrons. Ion pressure, on the other hand, is relatively higher in the premidnight sector because high-energy ions magnetic drift toward dusk. The opposite dawn-dusk asymmetries for ions and electrons result in relatively dawn-dusk symmetric total plasma pressure.

[20] Figure 6 shows how the midnight radial profiles and azimuthal profiles at $r = 11$–$12\ R_E$ at the two P_{SW} levels changes with Kp for $P_{t,n}$ and P_m. It can be seen that P_m profiles well represent the observed large-scale profiles and their systematical changes with increasing Kp and P_{SW}. Figure 7 shows direct and detailed comparisons of $P_{t,n}$ and P_m in their equatorial distributions and their radial and azimuthal profiles for four selected levels ($P_{SW} = 1.5$ and 3 nPa and $Kp = 1$ and 3). The fairly good overall agreement shown in Figures 6 and 7 (with the exception of $Kp = 5$ cases in the tail plasma sheet as indicated by the larger errors in the tables) indicates that observed pressure is well represented by the model pressure. Note that there is a discontinuity in $P_{t,n}$ at $r \sim 7\ R_E$, which is artificially due to the P_{SW} normalization being done only to data outside $r = 7\ R_E$. The model pressure inside $r = 10\ R_E$ and its change with Kp are also consistent with previous Active Magnetospheric Particle Tracer Explorers (AMPTE)/Charge Composition Explorer (CCE) observations [*Lui*, 2003].

3.2. Pressure Gradients and Comparison With Simultaneous THEMIS Measurement

[21] It is the pressure gradient in the force balance equation that determines a magnetic field configuration. Figure 8a shows the radial profiles of the radial pressure gradient (dP/dr) of P_m at midnight. Like the pressure profiles shown in Figure 7, pressure gradient increases with decreasing r with an order of

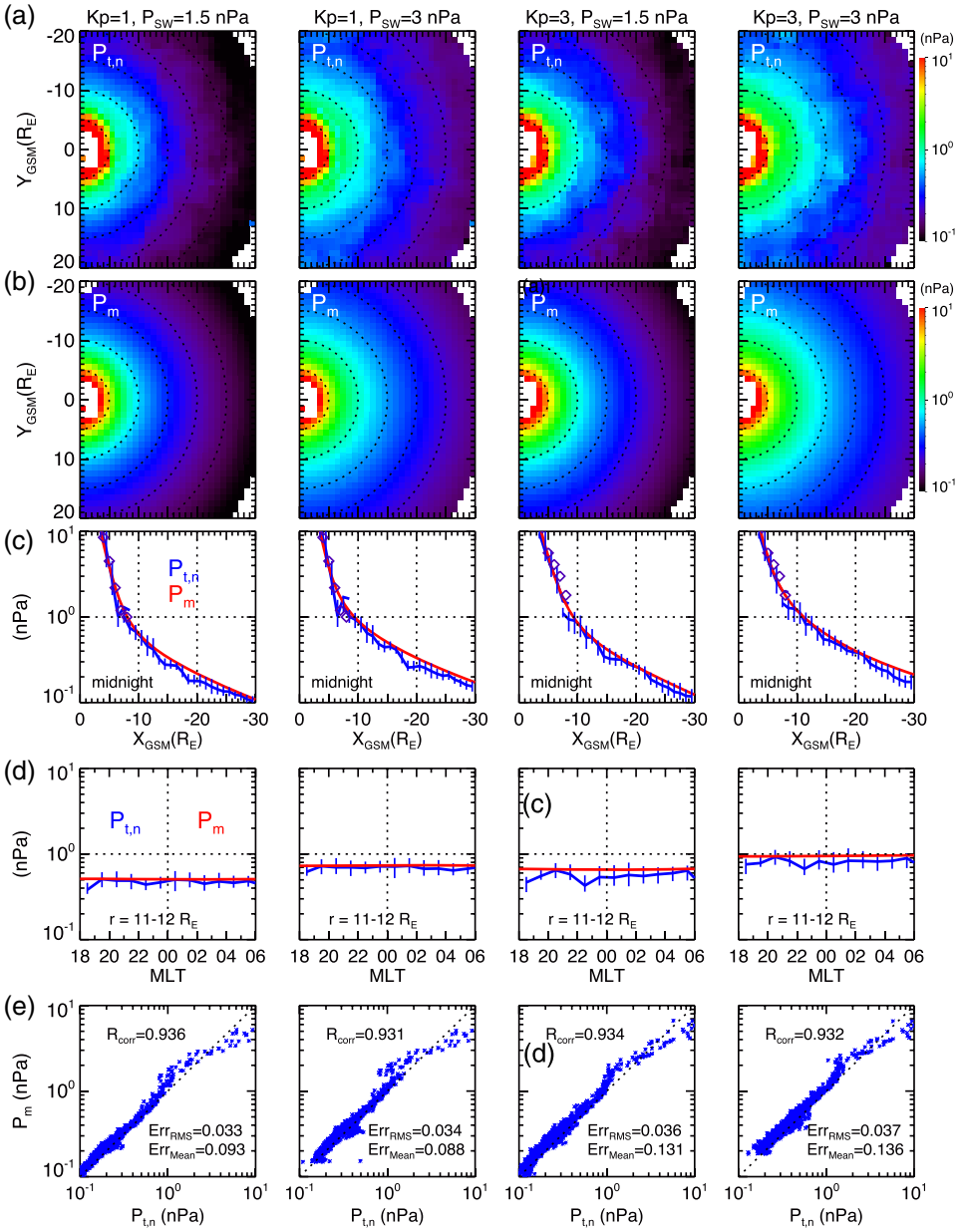

Figure 7. Equatorial distributions of (a) the normalized total pressure ($P_{t,n}$) and (b) the empirical model pressure (P_m). Comparisons between the normalized pressure (the blue curves) and model pressure (the red curves) in (c) the midnight radial profiles and (d) the azimuthal profiles at $r = 11$–12 R_E for $Kp = 1$ and 3 and $P_{SW} = 1.5$ and 3 nPa. The diamonds in Figure 7c are AMPTE/CCE observations from *Lui* [2003] for $Kp < 2$ (in the two $Kp = 1$ plots) and for $Kp > 3^+$ (in the two $Kp = 3$ plots).

magnitude increase from $X = -30$ to -10 R_E. The changes of dP/dr with Kp and P_{SW} vary with X. As Kp changes from 1 to 3, dP/dr increases by a factor of ~1.2 at $X = -30$ R_E while a larger increase of a factor of ~1.5 is seen at $X = -10$ R_E. An opposite X dependence is seen associated with the P_{SW} effect. As P_{SW} doubles from 1.5 to 3 nPa, a larger increase is seen at larger r (a factor of ~1.3 to 1.4 at $X < -20$ R_E) than at smaller r (a factor of ~1.2 at $X = -10$ R_E). This is due to the fact that P_t in the tail is better correlated with P_{SW} than in the near Earth. The above quite different dP/dr responses to Kp and P_{SW} result in characteristic differences in the corresponding changes of current density and magnetic field configuration as discussed in Paper 2.

[22] Figure 8b shows the MLT profiles of the azimuthal gradient (dP/dφ) of P_m at $r = 11.5$ R_E (positive dP/dφ means an eastward pressure gradient). dP_m/dφ is in the order of 10^{-4} nPa/R_E, which is 2 to 3 orders of magnitudes smaller than dP/dr. Therefore, statistically, there are almost no azimuthal pressure variations. As discussed in section 3.3, this is different from the empirical pressure profile of *Tsyganenko and Mukai* [2003], which has relatively lower pressure at midnight than at other MLTs.

[23] It is important that our model pressure from the statistical pressure profiles can provide realistic pressure gradients. As in *Xing et al.* [2009, 2011], instantaneous pressure gradients can be computed from the pressure simultaneously

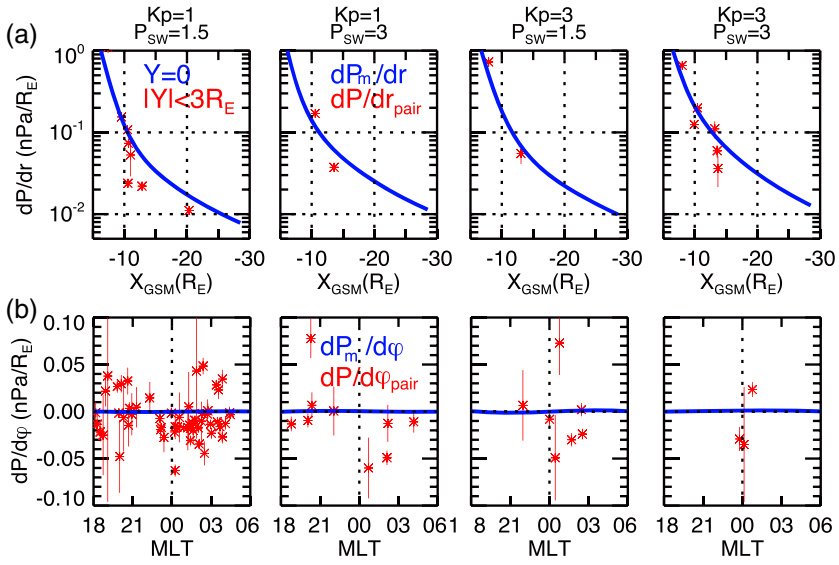

Figure 8. (a) The midnight radial profiles of dP/dr and (b) the MLT profiles of dP/dφ at r =11–12 R_E of the model pressure (the blue curves). The red dots are gradients computed from the pressure measurements simultaneously measured by two of the THEMIS spacecraft (with dot indicating the average over a 10 min period and vertical line indicating the standard deviation).

measured by any two of the five THEMIS spacecraft. To compute a pressure gradient from a THEMIS pair, we selected a pair with both spacecraft being in the region of plasma beta ≥ 1 and $|V_\perp| \leq 100$ km/s. To select data for reliable assessment of dP/dr, we required the MLT separation between the two spacecraft to be $\leq 5^o$ (1/3 MLT) and the radial separation (radial distance is $\sqrt{X^2+Y^2}$) to be between 0.9 and 5 R_E and also be larger than their azimuthal separation. For dP/dφ, their radial separation has to be between 0.5 and 1 R_E and be smaller than their azimuthal separation. P_t is used to represent the equatorial plasma pressure but without the normalization to a fixed P_{SW}. Despite three of the THEMIS spacecraft staying closely to each other most of the time, there are only few short periods when their alignment satisfies the above criteria. Nevertheless, data from these periods are valuable for evaluating our model pressure gradients.

[24] The pressure gradients observed by the THEMIS pairs are also shown in Figure 8. Each red dot represents an average of the pressure gradients within a 10 min period with the standard deviation indicated by the red vertical line. For dP/dr, most of the observed gradients are quite close to the model gradients, indicating that the P_m can give quite realistic radial pressure gradients. For dP/dφ, the magnitude of each of the observed gradients is much larger than the model gradients and can be even comparable to dP/dr. However, the observed gradient points are scattered around zero, implying that statistically there would be no significant azimuthal gradients, as predicted by P_m.

3.3. Comparison With Previous Empirical Models

[25] *Spence and Kivelson* [1993] established an empirical model for the midnight plasma pressure for r = 2 to 35 R_E for Kp = 1 using the plasma sheet observations from *Spence et al.* [1989]. A more sophisticated empirical model for r = 10 to 50 R_E controlled by the solar wind conditions (IMF and P_{SW}) was established by *Tsyganenko and Mukai* [2003] using Geotail observations. However, pressure from ions above 40 keV and from electrons is not included in the *Spence and Kivelson* pressure (P_{SK}) nor the *Tsyganenko and Mukai* pressure (P_{TM}).

[26] Figure 9a shows the comparisons between our model pressure (P_m) and those from the above two models. The

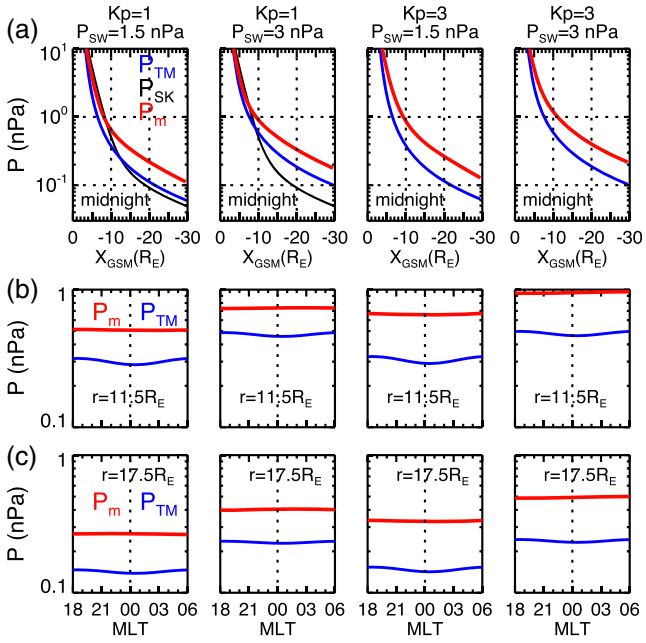

Figure 9. (a) Comparisons of the midnight radial profiles of pressure from our model (the red curves), the *Tsyganenko and Mukai* [2003] model (the blue curves), and the *Spence and Kivelson* [1993] model (the black curves). Comparisons of the MLT profiles between our model and the *Tsyganenko and Mukai* [2003] model at (b) r = 11.5 and (c) r = 17.5 R_E.

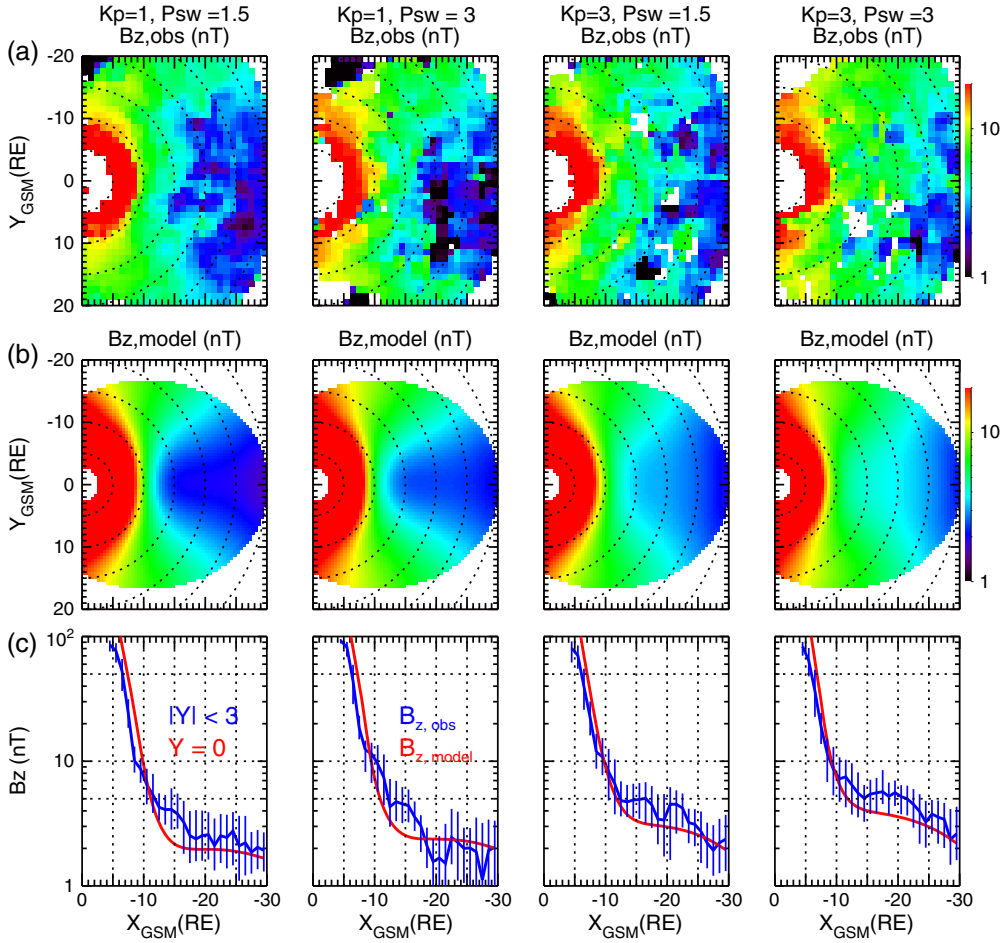

Figure 10. Equatorial distributions of (a) observed B_z and (b) model force-balanced B_z from Paper 2. (c) Comparisons of the radial profiles of observed B_z (the blue curves) and the model B_z (the red curves) near the midnight MLT.

IMF and P_{SW} inputs for the P_{TM} for $Kp = 1$ and 3 are specified using the median values indicated by the vertical dashed lines in Figure 1. For $Kp = 1$ and $P_{SW} = 1.5$ nPa, P_{SK} is similar to P_{TM} but both are almost a factor of 2 smaller than P_m. For $Kp = 3$, P_m remains a factor of ~2 higher than P_{TM}. Nevertheless, P_m and P_{TM} both show that plasma sheet pressure increases by a factor of ~1.6 as P_{SW} doubles.

[27] The azimuthal variations of P_m at $r = 11.5$ and 17.5 R_E are compared with those of P_{TM} in Figures 9b and 9c. P_{TM} shows clear azimuthal pressure gradient with relatively lower pressure at midnight. In addition to not including pressure from ions above 40 keV and electrons, the reason for relatively lower pressure from P_{SK} and P_{TM} than our results is also likely due to data selection. As shown in Figure 3, plasma pressure decreases with decreasing plasma beta. Even for plasma beta > 1, plasma pressure away from equator can be substantially lower than the pressure right at the equator. P_{SK} included all plasma pressure data regardless of the plasma beta and P_{TM} used plasma pressure data with plasma beta ≥ 1; thus, they are lower than our pressure that used total pressure with plasma beta ≥ 1 in the plasma sheet. Since the magnetic field is more stretched at midnight compared with other MLTs, plasma pressure falls off more quickly with decreasing plasma beta. This difference likely causes P_{TM} to be lower at midnight than other MLTs even though the same beta ≥ 1 criterion was used at all MLTs. As discussed in section 3.3 of Paper 2, the azimuthal pressure gradient is important to the generation of field-aligned currents (FACs). Thus, the azimuthal pressure gradient from P_{TM} may give rise to unrealistic FACs.

3.4. Comparisons of Observed Magnetic Field With Force-Balanced Magnetic Field

[28] Figures 10a and 10b show comparisons between the equatorial distributions of observed B_z near the equatorial plane (beta > 5) and the model B_z at $Z = 0$ from the force-balanced magnetic field obtained in Paper 2. The observed B_z in the plasma sheet for all Kp and P_{SW} is relatively lower at midnight than near the flanks, and the overall B_z in the plasma sheet increases with increasing Kp and P_{SW}. One exception is seen in the B_z near midnight beyond $X = -20$ R_E for $Kp = 1$ as it appears to decrease, rather than increase, with increasing P_{SW}. The model B_z reproduces reasonably well the spatial distributions and their overall response to Kp and P_{SW}. Figure 10c shows that the model Bz in the plasma sheet outside r ~10 R_E increases with decreasing r rather slowly for $Kp = 1$ but faster for $Kp = 3$, which agrees

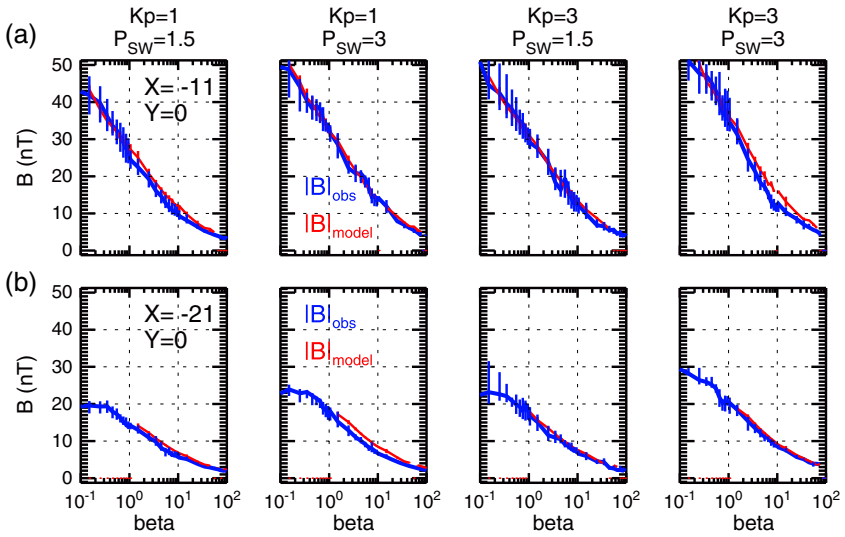

Figure 11. Total magnetic field as a function of plasma beta at (a) $X=-11$, $Y=0$ R_E and (b) $X=-20$ and $Y=0$ R_E for the observed (the blue curves) and model magnetic field (the red curves).

generally well with the observed radial variations with slightly lower magnitudes than the observations.

[29] To evaluate the model magnetic field variations in the Z direction, we plot in Figure 11 how $|B|$ changes with plasma beta in the model and the observations. Plasma beta is used to represent Z variations since the exact Z distance to the equatorial plane cannot be determined in the observations and plasma beta decreases with increasing Z. Figure 11 shows that $|B|$ at lower beta (higher Z) increases with increasing Kp with larger increase seen at smaller r. Compared with the Kp effect, there are more significant increases with increasing P_{SW} and the increases are seen throughout the plasma sheet. The model $|B|$ agrees fairly well with the observations, in both magnitudes and their responses to Kp and P_{SW}. Therefore, our empirical pressure and the associated force-balanced magnetic field can well represent the observed 3-D plasma pressure and magnetic field configurations and their dependences on Kp and P_{SW}.

4. Summary

[30] We have established an empirical model using Geotail and THEMIS data to best represent the spatial distribution of equatorial isotropic plasma pressure from $r=3$ to 30 R_E on the nightside magnetosphere for $Kp=0$ to 5 and for $P_{SW}=1.5$ and 3 nPa. The empirical pressure provides the realistic pressure constraint for constructing 3-D force-balanced magnetic field configurations presented in Paper 2.

[31] Unlike previous empirical models, we used plasma pressure plus radial magnetic pressure to represent equatorial plasma pressure. We also included pressure from high-energy ions as well as from electrons, which are important pressure contributors in the near-Earth region. This allows our pressure model to provide more accurate pressure gradients for our magnetic field modeling. Our empirical pressure profiles well represent the statistical spatial distributions with very high correlation coefficients. Compared with pressure gradients computed using simultaneous measurements from two THEMIS spacecraft, our model also gives reasonable radial and azimuthal pressure gradients.

[32] The pressure change with increasing Kp is characteristically different from the change with increasing P_{SW}. Larger convection electric field during higher Kp moves the plasma sheet further ward, resulting in larger increases in pressure and the radial pressure gradients in the near Earth compared to the tail region. On the other hand, magnetosphere compression by higher P_{SW} enhances pressure and radial pressure gradients more significantly in the tail region. While both pressure and radial gradients are enhanced with increasing Kp or P_{SW}, no significant azimuthal pressure variations are found statistically for all Kp and P_{SW} conditions.

[33] The observed equatorial B_z for all Kp and P_{SW} conditions increases with decreasing r slightly in the tail plasma sheet but strongly in the near-Earth region. Across the tail, the equatorial Bz is relatively lower near midnight than near the flanks. The overall Bz increases in the tail but decreases in the near-Earth region with increasing Kp or P_{SW}, and the changes are more significant with the Kp change. The total B at a fixed r for all conditions increases with increasing Z as indicated by the decreasing plasma beta. The increase becomes sharper during higher Kp or P_{SW}, and stronger increase is seen with increasing P_{SW}. Comparing these observed magnetic field profiles with the force-balanced magnetic field obtained in Paper 2 shows fairly good agreement, indicating our equilibrium model can well present realistic 3-D plasma and magnetic field configurations. The model accuracy in the inner magnetosphere can be further improved in the near future when more reliable pressure measurements become available from the recently launched Van Allen probes and anisotropic pressure is taken into account in the force-balanced magnetic field.

[34] **Acknowledgments.** The work by C.-P. Wang, C. Yue, X. Xing, and L. R. Lyons has been supported by NASA grant NNX11AJ12G and NNX12AD11G and NSF grant ATM-0819864 and ATM-1003595. The work by S.G. Zaharia has been supported by NSF grants 1131873 and 1203460, NASA grant NNH10AP09I, and by the IGPPS Program at Los Alamos National Laboratory. We acknowledge NASA contract NAS5-02099 for THEMIS, and C.W. Carlson and J.P. McFadden for the use of ESA data, D. Larson and R.P. Lin for use of the SST data, and K.H. Glassmeier, U. Auster, and W. Baumjohann for the use of FGM data provided under DLR contract 50 OC 0302. The work by A.T. Lui has been

supported by NASA grant NNX12AP62G to the Johns Hopkins University Applied Physics Laboratory. We thank T. Mukai at ISAS and CDAWeb for the use of the Geotail LEP data. The Geotail magnetic field data are provided through the DARTS system by ISAS. We thank Jon Vandegriff of the Applied Physics Laboratory for providing the Geotail EPIC data. We thank J.H. King, N. Papatashvilli at AdnetSystems, NASA GSFC, and CDAWeb for providing the OMNI data. *Kp* index was provided by World Data Center for Geomagnetism, Kyoto. We thank the support of ISSI International Teams Program: Plasma Entry and Transport in the Plasma Sheet.

[35] Masaki Fujimoto thanks the reviewers for their assistance in evaluating this paper.

References

Angelopoulos, V., C. F. Kennel, F. V. Coroniti, R. Pellat, M. G. Kivelson, R. J. Walker, C. T. Russell, W. Baumjohann, W. C. Feldman, and J. T. Gosling (1994), Statistical characteristics of bursty bulk flow events, *J. Geophys. Res.*, *99*(A11), 21,257–21,280.

Auster, H. U., et al. (2008), The THEMIS fluxgate magnetometer, *Space Sci. Rev.*, *141*, 235–264, doi:10.1007/s11214-008-9365-9.

Baumjohann, W. J., G. Paschmann, T. Nagai, and H. Lühr (1991), Superposed epoch analysis of the substorm plasma sheet, *J. Geophys. Res.*, *96*, 11,605–11,608.

Borovsky, J. E., M. F. Thomsen, and R. C. Elphic (1998), The driving of the plasma sheet by the solar wind, *J. Geophys. Res.*, *103*(A8), 17,617–17,640.

De Michelis, P., I. A. Daglis, and G. Consolini (1999), An average image of proton plasma pressure and of current systems in the equatorial plane derived from AMPTE/CCE-CHEM measurements, *J. Geophys. Res.*, *104*(A12), 28,615–28,624, doi:10.1029/1999JA900310.

Guild, T., et al. (2004), Plasma sheet climatology: Geotail observations and LFM model comparisons, *J. Atmos. Sol. Terr. Phys.*, *66*(15–16), 1351–1360.

Huang, C. Y., and L. A. Frank (1986), A statistical survey of the central plasma sheet: Implications for substorm models, *Geophys. Res. Lett.*, *13*, 652–655.

Kaufmann, R. L., C. Lu, W. R. Paterson, and L. A. Frank (2002), Three-dimensional analyses of electric currents and pressure anisotropies in the plasma sheet, *J. Geophys. Res.*, *107*(A7), 1103, doi:10.1029/2001JA000288.

Kaufmann, R. L., W. R. Paterson, and L. A. Frank (2004), Pressure, volume, density relationships in the plasma sheet, *J. Geophys. Res.*, *109*, A08204, doi:10.1029/2003JA010317.

Kirpichev, I. P., and E. E. Antonova (2011), Plasma pressure distribution in the equatorial plane of the Earth's magnetosphere at geocentric distances of 6–10 RE according to the international THEMIS mission data, *Geomagn Aeron*, *51*(4), doi:10.1134/S0016793211040049.

Kistler, L. M., E. Möbius, W. Baumjohann, G. Paschmann, and D. C. Hamilton (1992), Pressure changes in the plasma sheet during substorm injections, *J. Geophys. Res.*, *97*, 2973–2983.

Kokubun, S., T. Yamamoto, M. H. Acuna, K. Hayashi, K. Shiokawa, and H. Kawano (1994), The Geotail magnetic field experiment, *J. Geomagn. Geoelectr.*, *46*, 7–21, doi:10.5636/jgg.46.7.

Lagarias, J. C., J. A. Reeds, M. H. Wright, and P. E. Wright (1998), Convergence properties of the Nelder-Mead simplex method in low dimensions, *SIAM J Optim*, *9*(1), 112–147.

Lui, A. T. Y. (2003), Inner magnetospheric plasma pressure distribution and its local time asymmetry, *Geophys. Res. Lett.*, *30*(16), 1846, doi:10.1029/2003GL017596.

Lui, A. T. Y., and D. C. Hamilton (1992), Radial profiles of quiet time magnetospheric parameters, *J. Geophys. Res.*, *97*, 19,325–19,332.

McFadden, J. P., C. W. Carlson, D. Larson, V. Angelopoulos, M. Ludlam, R. Abiad, B. Elliott, P. Turin, and M. Marckwordt (2008), The THEMIS ESA plasma instrument and in-flight calibration, *Space Sci. Rev.*, *141*, 277–302, doi:10.1007/s11214-008-9440-2.

Mukai, T., S. Machida, Y. Saito, M. Hirahara, T. Terasawa, N. Kaya, T. Obara, M. Ejiri, and A. Nishida (1994), The low energy particle (LEP) experiment onboard the Geotail satellite, *J. Geomagn. Geoelectr.*, *46*, 669–692, doi:10.5636/jgg.46.669.

Newell, P. T., V. A. Sergeev, G. R. Bikkuzina, and S. Wing (1998), Characterizing the state of the magnetosphere: Testing the ion precipitation maxima latitude (b2i) and the ion isotropy boundary, *J. Geophys. Res.*, *103*(A3), 4739–4745, doi:10.1029/97JA03622.

Sergeev, V. A., and B. B. Gvozdevsky (1995), MT-index – A possible new index to characterize the magnetic configuration of magnetotail, *Ann. Geophys.*, *13*, 1093–1103, doi:10.1007/s00585-995-1093-9.

Spence, H. E., and M. G. Kivelson (1993), Contributions of the low-latitude boundary layer to the finite width magnetotail convection model, *J. Geophys. Res.*, *98*, 15,487–15,496.

Spence, H. E., M. G. Kivelson, R. J. Walker, and D. J. McComas (1989), Magnetospheric plasma pressures in the midnight meridian: observations from 2.5 to 35 R_E, *J. Geophys. Res.*, *94*, 5264–5272.

Tsyganenko, N. A., and T. Mukai (2003), Tail plasma sheet models derived from Geotail particle data, *J. Geophys. Res.*, *108*(A3), 1136, doi:10.1029/2002JA009707.

Wang, C.-P., L. R. Lyons, T. Nagai, J. M. Weygand, and R. W. McEntire (2007), Sources, transport, and distributions of plasma sheet ions and electrons and dependencies on interplanetary parameters under northward interplanetary magnetic field, *J. Geophys. Res.*, *112*, A10224, doi:10.1029/2007JA012522.

Wang, C.-P., L. R. Lyons, R. A. Wolf, T. Nagai, J. M. Weygand, and A. T. Y. Lui (2009), The plasma sheet PV5/3 and nV and associated plasma and energy transport for different convection strengths and AE levels, *J. Geophys. Res.*, *114*, A00D02, doi:10.1029/2008JA013849.

Wang, C.-P., L. R. Lyons, T. Nagai, J. M. Weygand, and A. T. Y. Lui (2010), Evolution of plasma sheet particle content under different interplanetary magnetic field conditions, *J. Geophys. Res.*, *115*, A06210, doi:10.1029/2009JA015028.

Wang, C.-P., M. Gkioulidou, L. R. Lyons, R. A. Wolf, V. Angelopoulos, T. Nagai, J. M. Weygand, and A. T. Y. Lui (2011), Spatial distributions of ions and electrons from the plasma sheet to the inner magnetosphere: Comparisons between THEMIS-Geotail statistical results and the Rice convection model, *J. Geophys. Res.*, *116*, A11216, doi:10.1029/2011JA016809.

Weimer, D. R. (1995), Models of high-latitude electric potentials derived with a least error fit of spherical harmonic coefficients, *J. Geophys. Res.*, *100*(A10), 19,595–19,608, doi:10.1029/95JA01755.

Williams, D. J., R. W. McEntire, C. Schlemm II, A. T. Y. Lui, G. Gloeckler, S. P. Christon, and F. Gliem (1994), Geotail energetic particles and ion composition instrument, *J. Geomagn. Geoelectr.*, *46*, 39–57, doi:10.5636/jgg.46.39.

Wing, S., and P. T. Newell (1998), Central plasma sheet ion properties as inferred from ionospheric observations, *J. Geophys. Res.*, *103*, 6785–6800.

Xing, X., L. R. Lyons, V. Angelopoulos, D. Larson, J. McFadden, C. Carlson, A. Runov, and U. Auster (2009), Azimuthal plasma pressure gradient in quiet time plasma sheet, *Geophys. Res. Lett.*, *36*, L14105, doi:10.1029/2009GL038881.

Xing, X., L. R. Lyons, Y. Nishimura, V. Angelopoulos, E. Donovan, E. Spanswick, J. Liang, D. Larson, C. Carlson, and U. Auster (2011), Near-Earth plasma sheet azimuthal pressure gradient and associated auroral development soon before substorm onset, *J. Geophys. Res.*, *116*, A07204, doi:10.1029/2011JA016539.